Stem Cell Reports
Article

OPEN ACCESS

Patient iPSC-Derived Neurons for Disease Modeling of Frontotemporal Dementia with Mutation in *CHMP2B*

Yu Zhang,[1,*] Benjamin Schmid,[2] Nanett K. Nikolaisen,[1] Mikkel A. Rasmussen,[2] Blanca I. Aldana,[3] Mikkel Agger,[4] Kirstine Calloe,[5] Tina C. Stummann,[6] Hjalte M. Larsen,[1] Troels T. Nielsen,[7] Jinrong Huang,[8,9] Fengping Xu,[8,9] Xin Liu,[8,9] Lars Bolund,[10] Morten Meyer,[4] Lasse K. Bak,[3] Helle S. Waagepetersen,[3] Yonglun Luo,[10] Jørgen E. Nielsen,[7] The FReJA Consortium, Bjørn Holst,[2] Christian Clausen,[2] Poul Hyttel,[1] and Kristine K. Freude[1,*]

[1]Stem Cells and Embryology Group, Department of Veterinary Clinical and Animal Sciences, Faculty of Health and Medical Sciences, University of Copenhagen, 1870 Frederiksberg C, Denmark
[2]Bioneer A/S, 2970 Hørsholm, Denmark
[3]Neurometabolism Research Unit, Department of Drug Design and Pharmacology, Faculty of Health and Medical Sciences, University of Copenhagen, 2100 Copenhagen, Denmark
[4]Stem Cell and Developmental Neurobiology Group, Department of Neurobiology Research, University of Southern Denmark, 5000 Odense C, Denmark
[5]The Physiology Group, Department of Veterinary Clinical and Animal Sciences, Faculty of Health and Medical Sciences, University of Copenhagen, 1870 Frederiksberg C, Denmark
[6]H. Lundbeck A/S, 2500 Valby, Denmark
[7]Neurogenetics Clinic & Research Lab, Danish Dementia Research Centre, Department of Neurology, Rigshospitalet, University of Copenhagen, 2100 Copenhagen, Denmark
[8]BGI-Shenzhen, 518083 Shenzhen, China
[9]China National GeneBank-Shenzhen, BGI-Shenzhen, 518083 Shenzhen, China
[10]Danish Regenerative Engineering Alliance for Medicine (DREAM), Department of Biomedicine, Aarhus University, 8000 Aarhus C, Denmark
*Correspondence: yu.zhang@sund.ku.dk (Y.Z.), kkf@sund.ku.dk (K.K.F.)
http://dx.doi.org/10.1016/j.stemcr.2017.01.012

SUMMARY

The truncated mutant form of the charged multivesicular body protein 2B (CHMP2B) is causative for frontotemporal dementia linked to chromosome 3 (FTD3). CHMP2B is a constituent of the endosomal sorting complex required for transport (ESCRT) and, when mutated, disrupts endosome-to-lysosome trafficking and substrate degradation. To understand the underlying molecular pathology, FTD3 patient induced pluripotent stem cells (iPSCs) were differentiated into forebrain-type cortical neurons. FTD3 neurons exhibited abnormal endosomes, as previously shown in patients. Moreover, mitochondria of FTD3 neurons displayed defective cristae formation, accompanied by deficiencies in mitochondrial respiration and increased levels of reactive oxygen. In addition, we provide evidence for perturbed iron homeostasis, presenting an in vitro patient-specific model to study the effects of iron accumulation in neurodegenerative diseases. All phenotypes observed in FTD3 neurons were rescued in CRISPR/Cas9-edited isogenic controls. These findings illustrate the relevance of our patient-specific in vitro models and open up possibilities for drug target development.

INTRODUCTION

Frontotemporal dementia (FTD) is the second most common form of early-onset (<65 years) dementia, accounting for 5%–8% of total dementia cases. FTD is a neurodegenerative disorder with cognitive impairment affecting the frontal and/or temporal lobes of the brain associated with progressive brain atrophy (Rossor et al., 2010). FTD is clinically, neuropathologically, and genetically heterogeneous. One gene affected in familial cases is the charged multivesicular body protein 2B (*CHMP2B*) located on chromosome 3 (FTD3). Patients display global cortical and central brain atrophies, with no apparent amyloid plaque formation or conclusive hyperphosphorylated tau aggregates (Isaacs et al., 2011). Early behavioral changes include apathy, restlessness, disinhibition, and hyperorality. Late-stage behavioral changes include stereotype behavior, mutism, and dystonia (Isaacs et al., 2011). CHMP2B is a component of the endosomal sorting complex required for transport III (ESCRT-III) complex, which facilitates recycling or degradation of cell surface receptors (Chassefeyre et al., 2015). As such, the FTD3-causing mutation of *CHMP2B* affects functionality of the endosome. Mouse and *Drosophila* FTD3 animal models have yielded valuable in vivo insights into the dysfunction of the endosomal lysosomal system and pathologic progression (Ahmad et al., 2009; Ghazi-Noori et al., 2012). However, transgene integration and species-specific differences may contribute to observed phenotypes in such models. Hence, there is an emerging need for human FTD3 models. In addition, studying how *CHMP2B*, as a rare mutation, contributes to neurodegenerative disorders has not yet attracted broader attention. Consequently, a *CHMP2B* mutant cellular model could provide further insights into common underlying dysfunction of biological pathways, disrupted or disturbed in neurodegenerative diseases and thereby linking different forms of neurodegeneration.

The availability of viable neurons from patient brains, at least in part, limits the investigation of the mechanism of

This is an open access article under the CC BY-NC-ND license (http://creativecommons.org/licenses/by-nc-nd/4.0/).

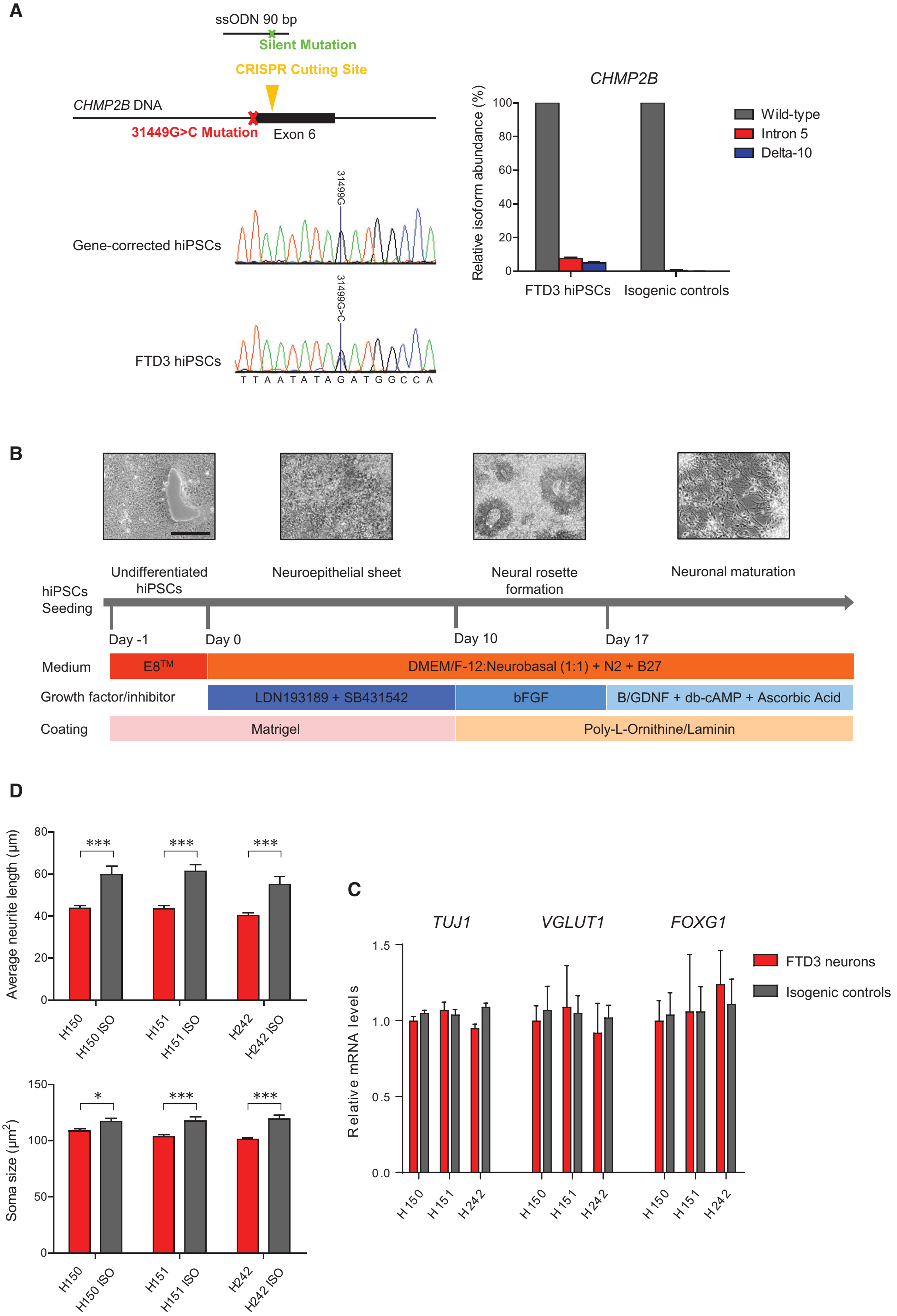

(legend on next page)

neurodegenerative pathogenesis. In this context, human-induced pluripotent stem cells (iPSCs) provide invaluable access to study the disease progression in neurons derived from patient iPSCs and facilitate the development of new therapies (Ehrlich et al., 2015; Rasmussen et al., 2014). Meanwhile, recent advances of state-of-the-art genome engineering technique CRISPR/Cas9 (Ran et al., 2013) have had a tremendous impact allowing for gene correction in patients who are carriers of disease-causing single-point mutations. Such genetically edited iPSCs are ideal isogenic controls for the patient-derived iPSCs, allowing to precisely dissect the significance of the disease-causing mutation while maintaining the patient's own genetic background.

To study the cellular and molecular events of FTD3, we derived a disease model using human iPSCs from patients carrying the 31449G > C mutation in *CHMP2B* and isogenic controls generated via the CRISPR/Cas9 system with subsequent in vitro neuronal differentiation. Our model not only confirmed partly prior-observed pathologies in animal models such as endosome dysregulation (Ghazi-Noori et al., 2012), but also revealed additional disease-relevant phenotypes in FTD3 by way of abnormal mitochondrial ultrastructure and function. Moreover, RNA sequencing (RNA-seq) uncovered that the *CHMP2B* mutation manifests in dysregulated expression of key genes associated with Parkinson's disease (PD) and Alzheimer's disease (AD) and indicated that perurbed iron homeostasis is one of the underlying disease mechanisms.

RESULTS

Generation of FTD3 iPSCs and Genetically Corrected Isogenic Controls

Skin fibroblasts from two symptomatic FTD3 patients (H150 and H151) and one presymptomatic FTD3 patient (H242) were reprogrammed using non-integrative episomal plasmids. All of these individuals are from the same family, and one independent healthy control from an unrelated family was also included. Individual FTD3 iPSC lines were assessed for pluripotency features via qPCR (Figure S1A) and immunocytochemistry (ICC) (Figure S1B). Assessment of pluripotency potential was confirmed via embryoid body formation and subsequent spontaneous differentiation (Figure S1C). The FTD3-causing mutation 31449G > C (located at the splice acceptor site in *CHMP2B*, at the border of intron 5 and exon 6) was repaired in the FTD3 iPSC lines using the CRISPR/Cas9 system (Figure 1A). The presence of altered *CHMP2B* mRNA, as formerly shown in Urwin et al. (2010) was confirmed via qPCR and showed expression of the intron 5 and delta-10 isoforms only in the patient iPSC. These abnormal transcripts, generated via the CHMP2B mutation affecting the slice acceptor site, are completely absent in the isogenic controls (Figure 1A). All iPSC and genetically corrected isogenic lines were determined to be karyotypically normal (Figure S1D).

Differentiation of FTD3 iPSCs to Forebrain Cortical Neurons

We employed a modified dual SMAD protocol (Figure 1B) to generate forebrain-specific cortical neurons. Flow cytometry analyses demonstrated the neural progenitor cell (NPC) cultures to be comparable with respect to NESTIN and SOX1 expression (Figure S2A). All NPCs expressed the forebrain markers PAX6 and OTX2 (Figure S2B). ICC revealed the majority of the matured neurons to be glutamatergic (immunopositive for VGlut1 [Figure S2C] and co-positive for MAP2, TAU, and TUJ1 [Figure S2C]). Approximately 10% of neurons were GABAergic (Figure S2C), while approximately 5% were GFAP-positive astrocytes, with a minor population (2%–3%) comprising tyrosine hydroxylase-positive dopaminergic neurons (Figure S2C). Since quantification via ICC is challenging we performed qPCR for *TUJ1*, *VGlut1*, and FOXG1 in order to estimate the comparability in regard to the neural cell composition of the investigated FTD3 iPSC- and isogenic iPSC-derived neurons. All lines showed comparable amounts of expression with no significant differences, which is also indicative that the mutation in *CHMP2B* does not affect the differentiation potential toward neurons (Figure 1C). Neurons exhibited spiking activity and action potentials, which occurred both spontaneously

Figure 1. Gene Correction of FTD3 iPSCs, In Vitro Neuronal Differentiation, and Morphometric Analyses

(A) CRISPR/Cas9-mediated gene correction of *CHMP2B* 31449G > C, ssODN with silent mutation (*Sac*II), sequencing results, and quantification of *CHMP2B* mutant and wild-type mRNA transcripts. The expression values were calculated as relative amount of mRNA versus expression values of wild-type which was set to 100%.

(B) Schematic of neuronal differentiation protocol (see Experimental Procedures for details). Scale bar, 200 μm for all. BFGF, basic fibroblast growth factor; GDNF, glial cell line-derived neurotrophic factor; cAMP, cyclic AMP.

(C) Quantification of *TUJ1*, *VGlut1*, and FOXG1 mRNA expression levels in FTD3 neurons (H150, H151, H242) and isogenic controls (H150 ISO, H151 ISO, H242 ISO). n = 3 with three replicates in each experiment, no significant differences were found among the different lines.

(D) Morphometric analyses in FTD3 neurons and isogenic controls: Average neurite length and soma size. n = 3 with three replicates in each experiment, significant differences are indicated by $^{*}p < 0.05$ and $^{***}p < 0.001$.

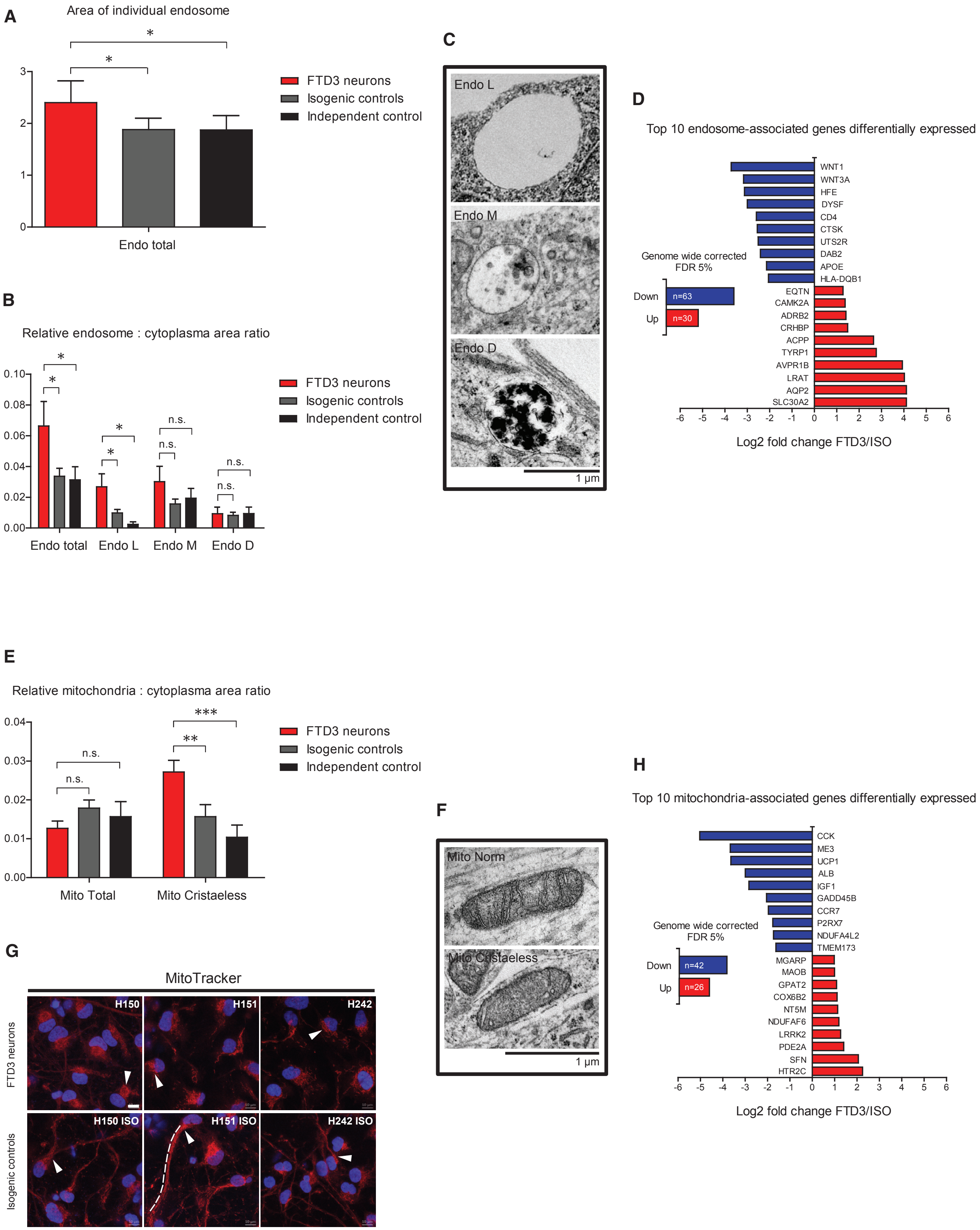

(legend on next page)

and under current-clamp conditions (Figures S3B–S3D). Measurement of intracellular calcium levels also demonstrated that cultures exhibited neuronal functionality. The neurons were responsive to the neurotransmitters glutamate/glycine, GABA, and, to a lesser extent, acetylcholine (Figure S3A), and depolarization of the plasma membrane by addition of potassium resulted in a small increase in intracellular calcium (Figure S3A). Serotonin and dopamine did not induce a change in intracellular calcium levels. All lines showed similar responses.

FTD3 Neurons Display Aberrant Endosomes

Via transmission electron microscopy, we observed similarly enlarged endosome (assessed as endosome-occupied relative neuronal area, see the Supplemental Experimental Procedures) in our FTD3 neurons, as previously demonstrated in patients (Urwin et al., 2010) (Figure 2A). Such enlarged endosomes were absent from the isogenic controls, indicating a rescue of the phenotype by CRISPR/Cas9-mediated gene correction and is consistent with previous knockdown experiments (Nielsen et al., 2012). Specifically, the electron-lucent and, thus, vacant endosomes were significantly more abundant in the FTD3 neurons (Figures 2B and 2C), indicative of an effect on early-stage endosomes.

FTD3 Neurons Display Abnormal Mitochondria

Given that mitochondrial defects are commonly observed in neurodegenerative diseases, we assessed whether such a phenotype is evident in FTD3 neurons. While we noted no apparent difference in size of mitochondria between FTD3 neurons and their isogenic controls, we did observe a significant increase in abnormal mitochondria with severe impairment of cristae formation in FTD3 neurons (Figures 2E and 2F). Strikingly, the distribution of mitochondria within neurons was also perturbed in FTD3 neurons: MitoTracker analyses revealed mitochondria in FTD3 neurons to preferentially localize to the perinuclear region, while isogenic controls exhibited a homogeneous distribution throughout axons and dendrites (Figure 2G). Consistent with previous studies correlating a lack of axonal mitochondria with axonal degradation (Rawson et al., 2014), we also observed disorganized microtubule organization in FTD3 neurons (Figure S4A). These findings were substantiated by the fact that the average neurite length and soma size were significantly reduced in FTD3 neurons versus isogenic controls (Figure 1D).

FTD3 Neurons Display Impaired Mitochondria Function and Increased Oxidative Stress

Prompted by our observations of aberrant mitochondrial morphology, we sought to test the functionality of such FTD3 mitochondria by assessing their basal respiration rate, ATP-linked respiration, proton leak, and reserve capacity. Our analyses uncovered a reduced basal respiration rate in FTD3 neurons as well as a reduced maximal capacity (Figure 3E). Consistent with mitochondrial dysfunction manifesting in oxidative stress, we observed up to 20% occurrence of oxidative stress in FTD3 neurons compared with only 7% in isogenic controls (Figure 3A). Thus, FTD3 neurons are exposed to higher levels of oxidative stress, and targeted gene editing can reverse the disease phenotype. Subsequently, we investigated whether the increased oxidative stress impacts cell viability, but we detected no evidence for increased apoptosis in FTD3 neurons (Figure 3B).

Global Gene Expression Analyses Confirm Defects in the Endosome, Mitochondrial Dysfunction, and Increased Oxidative Stress

To obtain an overview of gene expression changes in CHMP2B-dependent neurodegeneration, we performed

Figure 2. FTD3 Neurons Exhibit Aberrant Endosome and Mitochondria

(A and B) Stereology and ultrastructure of endosome in FTD3 neurons (red bar), isogenic controls (gray bar), and an independent healthy control (black bar): (A) shows total size of endosome; (B) shows the ratio of endosome to cytoplasm and further subdivision by appearance into electron-lucent (Endo L), medium electron-dense (Endo M), and electron-dense (Endo D); n = 3 with three replicates in each experiment, significant differences are indicated by $^{*}p < 0.05$. n.s., not significant.

(C) Transmission electron microscopy (TEM) images of Endo L, Endo M, and Endo (D) Scale bar, 1 μm for all.

(D) Total number of endosome-associated genes and the top ten differentially expressed genes (on the basis of fold-change) within a false discovery rate (FDR) of 5%.

(E) Stereology and ultrastructure of mitochondria in FTD3 neurons (red bar), isogenic controls (gray bar), and an independent healthy control (black bar): relative size of mitochondria compared with cytoplasmic area of all mitochondria (Mito total) and cristaeless mitochondria; n = 3 with three replicates in each experiment, significant differences are indicated by $^{**}p < 0.01$, and $^{***}p < 0.001$.

(F) TEM images of normal and cristaeless mitochondria. Scale bar, 1 μm for both.

(G) Images of neurons dyed with the mitochondrial probe MitoTracker (red) counterstained with DAPI (blue). Arrowheads indicate dyed mitochondria and the dashed line shows a representative distribution of mitochondria in an isogenic control neuron. Scale bar, 10 μm for all.

(H) Total number of mitochondria-associated genes and top ten differentially expressed genes (on the basis of fold-change) within an FDR of 5%.

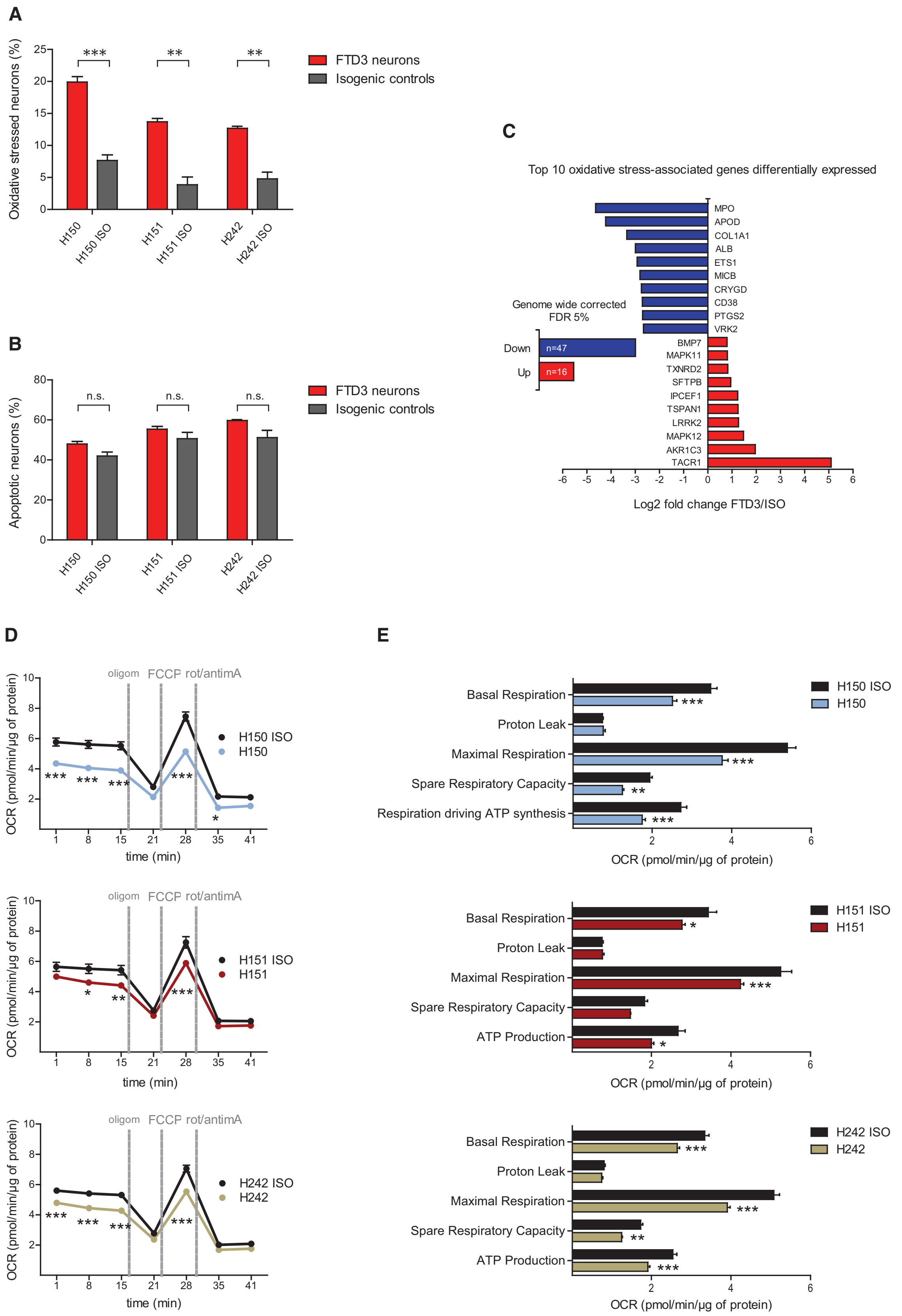

(legend on next page)

RNA-seq analyses, which revealed 3,205 differentially expressed genes in FTD3 neurons compared with their isogenic controls. Heatmap analyses showed that neurons derived from iPSCs of all three FTD3 individuals clustered together, while isogenic controls clustered together with the independent healthy individual (Figure 4A), suggesting that the isogenic control lines reverted to a healthy control gene expression profile after repair of the *CHMP2B* mutation. To identify which cellular components are primarily affected in FTD3 neurons, we performed gene ontology (GO) term analysis. We found enrichment of the GO term for postsynaptic membrane, synaptic membrane, neuron projection, and synaptic vesicle membrane (Figure 4C), and depletion of early endosome membrane, lysosomal lumen, and endocytic vesicle membrane (Figure 4D).

With the aim to identify additional genes associated with the main phenotypes observed in FTD3 neurons, we extracted the top ten differentially regulated genes functionally linked to neurodegeneration and associated with endosomes (Figure 2D), mitochondria (Figure 2H), and oxidative stress (Figure 3C). Strikingly, *APOE* ranked among the ten most downregulated endosome-associated genes (Figure 2D). APOE4, an isoform of APOE, is a well-known risk factor for sporadic AD (sAD) (Corder et al., 1993) and, consistent with a putative role in FTD3 pathophysiology, some sAD patients present with enlarged early endosomes (Cataldo et al., 2000).

Most interestingly, we observed an upregulation of leucine-rich repeat kinase 2 (*LRRK2*) among the mitochondria-related genes (Figure 2H). *LRRK2* is one of the five genes mutated in familial forms of PD. Previous studies reported mitochondrial fragmentation due to increased expression of *LRRK2* (Wang et al., 2012), pointing to an association between upregulated *LRRK2* expression and cristae dysgenesis in FTD3 neurons. *LRRK2* was also detected in the oxidative stress group (Figure 3C) and is upregulated in some cases of sporadic PD (Cho et al., 2013) accompanied by elevated levels of oxidative stress (Nguyen et al., 2011). *MPO* and *APOD*, both implicated in AD (Figure 3C) (Maki et al., 2009; Martinez et al., 2012), were strongly downregulated in FTD3 neurons.

Imbalance of Iron Homeostasis Represents a Unifying Factor Linking Endosome, Mitochondrial Dysfunction, and Oxidative Stress

Via our in silico analyses, we identified mis-expression of genes encoding proteins or receptors known to be involved in iron homeostasis. Among these were *TRPC6* (12-fold upregulated), *HFE* (8-fold downregulated), and *ABCG2*, *HP*, and *CP* (all 2-fold downregulated) (Figure 4B). A potential imbalance of iron homeostasis might plausibly induce intracellular ferrous iron (Fe^{2+}) accumulation, damaging mitochondria and inducing stress, to be further exacerbated by the defects in the endosome compartment contributing to increased amounts of trapped Fe^{3+} within endosomes (Figure 4E). Supporting this hypothesis, cytoplasmic Fe^{2+} levels are significantly increased in FTD3 neurons versus isogenic control neurons (Figure 4F). This increase in intracellular iron was consistent in several independent neural differentiation experiments, and the increased expression in TRCP6 was also confirmed via western blot analysis (Figure 4B), further substantiating our hypothesis for impaired iron homeostasis triggered by altered expression and protein amounts of key regulators.

Taken together we have shown that FTD3 neurons have enlarged early endosomes, display mitochondria dysfunction and perturbed iron homeostasis, with subsequent increase in oxidative stress.

DISCUSSION

The biological function of CHMP2B has primarily been investigated in animal models, with the attendant caveat that observed phenotypes are potentially species specific or contributed to by transgene integration. Here, to preclude such issues, we developed an FTD3 patient-derived disease model by way of iPSCs generation, genome editing, and in vitro neuronal differentiation techniques.

We identified enlargements of particularly the early endosome population in FTD3 neurons, indicating that perturbed endo-lysosomal fusion and degradation of substrates is key to the underlying FTD3 pathophysiology. Cellular

Figure 3. Impaired Mitochondrial Function and Oxidative Stress in FTD3 Neurons

(A) CellROX green and SYTOX red flow cytometry assay of live oxidative stressed neurons. n = 3 with three replicates in each experiment, significant differences are indicated by $^{**}p < 0.01$ and $^{***}p < 0.001$.

(B) CellEvent Caspase-3/7 green and SYTOX red flow cytometry assay of apoptotic neurons.

(C) Total number of oxidative stress-associated genes and the top ten differentially expressed genes (on the basis of fold-change) within an FDR of 5%. n.s., not significant.

(D and E) Mitochondrial function profile of FTD3 neurons (H150, H151 and H242) and isogenic controls (H150 ISO, H151 ISO, H242 ISO). (D) oxygen consumption rate (OCR) was measured before (basal) and after the addition of oligomycin (oligom), carbonyl cyanide-4-(trifluoromethoxy)phenylhydrazone (FCCP), and a mixture of rotenone (rot) and antimycin A (antimA), respectively; (E) mitochondrial respiration parameters were calculated based on the OCR measurements shown in (D) as described in the Supplemental Experimental Procedures. n = 3 with three replicates in each experiment, significant differences are indicated by $^{*}p < 0.05$, $^{**}p < 0.01$, and $^{***}p < 0.001$.

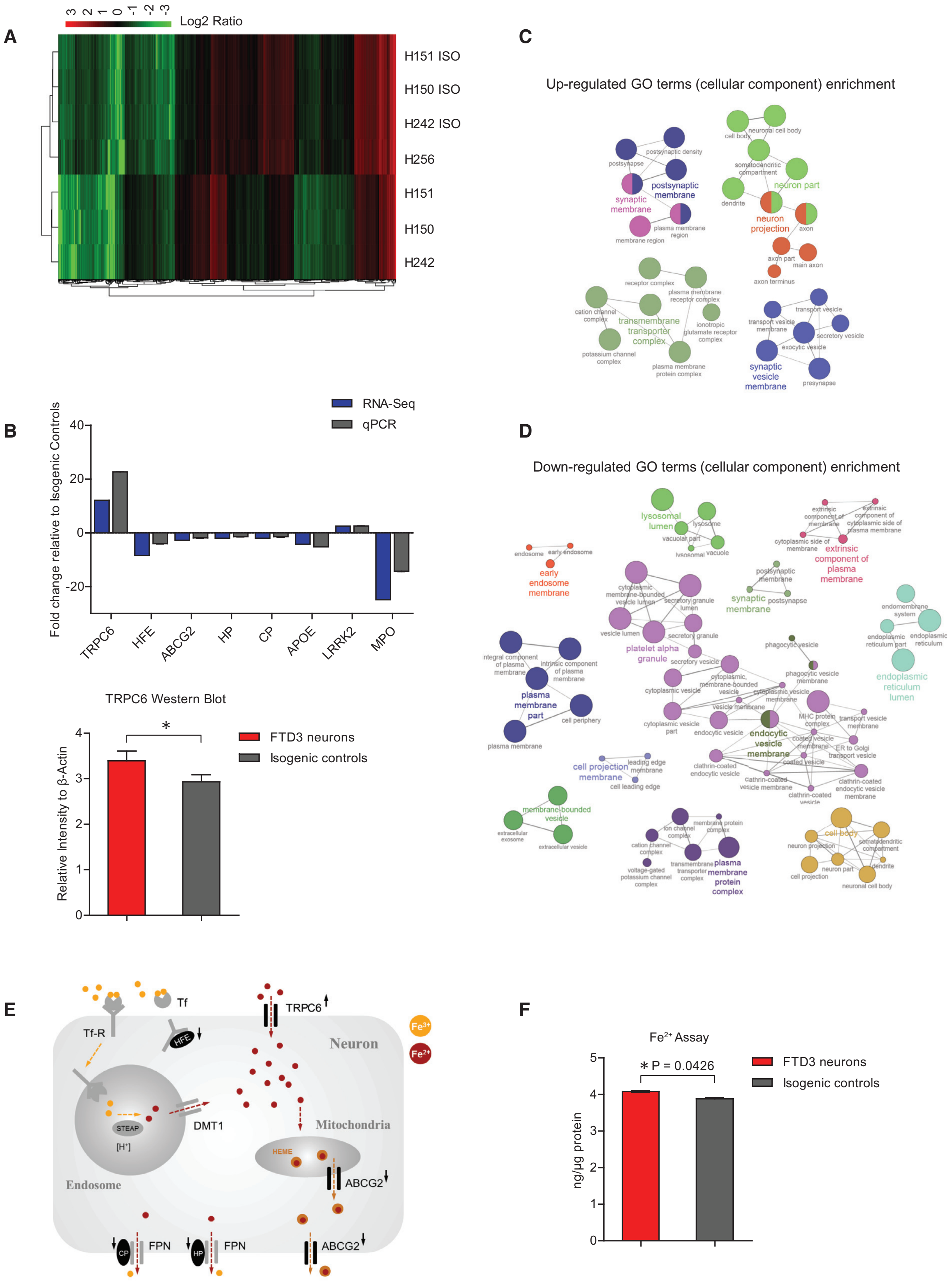

(legend on next page)

components, including mitochondria, are degraded in the endosome; in amyotrophic lateral sclerosis, a progressive lysosomal deficit is causative for impaired degradation of damaged mitochondria in motor neurons (Xie et al., 2015). Defective recycling of large organelles, such as mitochondria, is the earliest detectable impairment in a chain of events initiated by defective recycling (Cannizzo et al., 2012), which clearly links endosome and mitochondrial dysfunction.

FTD3 neurons displayed abnormal mitochondrial localization and cristae formation, manifesting in impaired functionality typical for neurodegenerative diseases. Defective mitochondria show impaired ATP generation and release of deleterious chemicals such as reactive oxygen species (ROS), potentially inducing cell death. We contend that increased ROS release contributes to increased organelle damage, which cannot be appropriately ameliorated through degradation owing to the observed endosome defects, resulting in a self-perpetuating cycle of cellular damage.

Strikingly, in FTD3 neurons we identified a robust, significant upregulation of *LRRK2* encoding the dardarin protein. One function of dardarin is the modulation of intracellular trafficking via recruitment of RAB7 (Greggio et al., 2006). Mutant CHMP2B impairs the recruitment of RAB7, crucial for endosome-lysosome fusion (Urwin et al., 2010). This relationship between CHMP2B, RAB7, and dardarin is supported by studies showing that dardarin negatively regulates RAB7-dependent localization of the lysosome (Dodson et al., 2012). Therefore, upregulation of *LRRK2* as a consequence of *CHMP2B* mutation might contribute to deficient endo-lysosomal trafficking and fusion. Dardarin also plays a role in mitochondrial functionality and positioning, since induced expression of *wild-type LRRK2* induces mitochondrial fragmentation via increased fission and upregulation of *DLP1*, which is critical for correct mitochondrial distribution (Wang et al., 2012).

Furthermore, our analysis revealed *APOE* to be significantly downregulated in FTD3 neural cells. The cells analyzed via RNA-seq are a mixed population of neurons and glial cells, with an up to 90% enrichment of VGlut1$^+$ neurons. Due to this mixed population of cells we were still able to detect *APOE* via RNA-seq, even though it is mainly expressed in astrocytes. APOE is a major cholesterol carrier in neurons that supports lipid transport and brain injury repair, and there is a key requirement for APOE in facilitating the clearance of soluble amyloid beta (Abeta) (Jiang et al., 2008). Furthermore, APOE suppresses microglia activation (Laskowitz et al., 2001), and reduced APOE levels might potentially trigger inflammatory events. Together, this suggests that downregulation of APOE in FTD3 neurons might be a contributing factor in the microglia activation seen in postmortem FTD3 brains. Interestingly, we observed another phenotype restricted to glial cells. It has previously been reported for FTD3 mouse models and patient brains that these display p62 inclusions, which are indicative for impaired autophagy, oxidative stress, and neurotoxicity (Ghazi-Noori et al., 2012; Holm et al., 2007). We identified these p62 inclusions only in the S100β$^+$ glial cell population and not in our TUJ1$^+$ neurons (Figure S4B). Both the APOE and the p62 phenotypes clearly show that, even though several disease features can be replicated in our FTD3 neurons, other neural cell types need to be investigated in the future to understand the full complexity and pathophysiology of the disease.

Based on the differentially expressed key components and increase of intracellular iron in FTD3 neurons, we present an additional pathological feature of FTD3, which is associated with an imbalance in iron homeostasis (Figure 4E). Iron uptake principally proceeds through iron bound to transferrin mediated via the transferrin receptor or via direct uptake of Fe^{2+} facilitated by a variety of receptors including TRPC6 (Mwanjewe and Grover, 2004). We propose that upregulation of TRPC6 manifests in increased uptake of Fe^{2+}, while downregulation of HFE (which competes with Tf), results in uptake of more ferric iron which can further be reduced into Fe^{2+}. In contrast, export of heme-bound iron via ABCG2 or unbound Fe^{2+} through FPN can be reduced. Concordant with this model, we confirmed in several individual differentiation experiments a small but significant increase of intracellular iron within 5 weeks of neuronal differentiation in FTD3 neurons. Excessive amounts of intracellular Fe^{2+} are toxic to

Figure 4. Transcriptional Analysis of FTD3 Neurons Versus Isogenic Controls and Quantification of Intracellular Fe^{2+} Content

(A) Heatmap and hierarchical clustering analysis of gene expression profile of FTD3 neurons (H150, H151, H242) and isogenic controls (H150 ISO, H151 ISO, H242 ISO) as well as one independent healthy control (H256).

(B) qPCR validation of genes of interest from RNA-seq results and western blot relative quantification of TRPC6 protein expression.

(C and D) GO term enrichment analysis of differentially expressed genes via ClueGO v1.4 software. Functionally grouped network with terms as nodes linked based on their kappa score level (≥ 0.5), where only the label of the most significant term per group is shown. The node size represents the term enrichment significance. Functionally related groups partially overlap.

(E) Diagram of key dysregulated genes involved in intracellular iron homeostasis.

(F) Fe^{2+} assay and concentration normalized to total cellular protein.n = 3 with three replicates in each experiment, significant differences are indicated by $^*p < 0.05$.

cells and trigger the production of ROS. Moreover, Fe^{2+} and hydrogen peroxide engage in the so-called Fenton reaction, producing ferric iron and highly reactive hydroxide, which damages DNA, proteins, and lipids in the cell (Altamura and Muckenthaler, 2009).

FTD3 neurons present with enlarged early endosomes, increased cristaeless mitochondria, intracellular iron accumulation, and oxidative stress. All of these phenotypes were rescued via genetic correction of the CHMP2B mutation.

We propose that in FTD3 neurons two events occur in parallel: (1) mutant CHMP2B causes an imbalance in iron homeostasis triggering mitochondrial impairment, which consequently triggers ROS and neuronal damage, and (2) mutant CHMP2B-dependent enlargement of endosomes, which causes defects of the endo-lysosomal degradation and recycling pathway, including recycling of receptors for iron uptake, results in accumulation of defective mitochondria, imbalanced iron homeostasis, ROS, and neuronal damage. Future studies will determine the exact role of mutant CHMP2B on a molecular level within these cellular events.

In conclusion, our findings indicate a possibility of targeting iron imbalances therapeutically in efforts to intervene in this cycle of damage to attempt treatment of FTD3. Furthermore, the CHMP2B-dependent human iPSC-derived neurons can be added to the list of in vitro cellular model systems that serve as a tool to study not only common mechanisms of pathogenesis, such as mitochondrial defects and oxidative stress, but also the effects of iron accumulation in neurodegenerative diseases.

EXPERIMENTAL PROCEDURES

Cell Culture, iPSC Generation, and Neuronal Differentiation

iPSCs were generated via episomal reprogramming (Addgene, 27077, 27078, 27080) from human dermal fibroblasts obtained from skin biopsies. Neuronal differentiation followed a modified dual SMAD protocol.

Genome Editing

Generation of isogenic controls from the three FTD3 iPSC lines was achieved via the CRISPR/Cas9 system (Addgene, 62988) using single-strand donor oligonucleotides as a template.

Transmission Electron Microscopy

Cells were seeded on 13 mm Thermanox plastic coverslips (Nunc, 174950) coated with poly-O-Lysine/laminin. Ultra-thin (50–70 nm) sections were prepared, contrasted with 2% uranyl acetate (PolyScience, 21447) and lead citrate, and examined using a Philips CM100 transmission electron microscope equipped with a Morada camera.

RNA-Seq Analysis

For deep RNA-seq, libraries of FTD3 neurons, isogenic controls, and an independent healthy control were prepared and sequenced on a HiSeq 2000 Sequencing System (Illumina) following the manufacturer's protocol.

Statistical Analysis

Data are presented as mean ± SE. n is the number of independent differentiations of NPCs (from the cryobank) to neurons. Significance of data was evaluated by Student's t test or two-way ANOVA with Bonferroni post hoc test. Unless noted otherwise, $p < 0.05$ was considered statistically significant.

For further details on Experimental Procedures, see the Supplemental Information.

ACCESSION NUMBERS

The RNA-seq data described in this study have been deposited in the NCBI GEO database under accession number GEO: GSE92340.

SUPPLEMENTAL INFORMATION

Supplemental Information includes Supplemental Experimental Procedures, four figures, and one table and can be found with this article online at http://dx.doi.org/10.1016/j.stemcr.2017.01.012.

AUTHOR CONTRIBUTIONS

Y.Z. and K.K.F. designed the study. Y.Z., B.S., N.K.N., M.A.R., B.I.A., M.A., K.C., T.C.S., H.M.L., T.T.N., J.H., F.X., X.L., L.B., M.M., L.K.B., H.S.W., Y.L., J.E.N., The FReJA Consortium, B.H., C.C., P.H., and K.K.F. conducted the experiments and interpreted the results. Y.Z. and K.K.F. wrote the manuscript.

ACKNOWLEDGMENTS

This work was supported by awards from: EU FP7 Marie Curie Industry-Academia Partnerships and Pathways (IAPP) grant (STEMMAD, PIAPP-GA-2012-324451), Innovation Fund Denmark (BrainStem, 4108-00008B), Lundbeck Foundation (R151-2013-14439) (L.B.), Danish Research Council for Independent Research (DFF-1337-00128 and DFF-1335-00763) (Y.L.), China Scholarship Council (Y.Z.), and Ministry of Science, Technology and Innovation of Mexico (B.I.A.). We are grateful to the FTD3 family for their support of this work. Finally, we would like to thank Ms. Hanne Holm and Tina Christoffersen from the University of Copenhagen, Ms. Ulla Poulsen from Bioneer A/S, and Mr. Lingfei Ye from BGI-Shenzhen for expert technical assistance.

Received: August 27, 2016
Revised: January 16, 2017
Accepted: January 17, 2017
Published: February 16, 2017

REFERENCES

Ahmad, S.T., Sweeney, S.T., Lee, J.A., Sweeney, N.T., and Gao, F.B. (2009). Genetic screen identifies serpin5 as a regulator of the toll pathway and CHMP2B toxicity associated with frontotemporal dementia. Proc. Natl. Acad. Sci. USA *106*, 12168–12173.

Altamura, S., and Muckenthaler, M.U. (2009). Iron toxicity in diseases of aging: Alzheimer's disease, Parkinson's disease and atherosclerosis. J. Alzheimers Dis. *16*, 879–895.

Cannizzo, E.S., Clement, C.C., Morozova, K., Valdor, R., Kaushik, S., Almeida, L.N., Follo, C., Sahu, R., Cuervo, A.M., Macian, F., et al. (2012). Age-related oxidative stress compromises endosomal proteostasis. Cell Rep. *2*, 136–149.

Cataldo, A.M., Peterhoff, C.M., Troncoso, J.C., Gomez-Isla, T., Hyman, B.T., and Nixon, R.A. (2000). Endocytic pathway abnormalities precede amyloid beta deposition in sporadic Alzheimer's disease and Down syndrome: differential effects of APOE genotype and presenilin mutations. Am. J. Pathol. *157*, 277–286.

Chassefeyre, R., Martinez-Hernandez, J., Bertaso, F., Bouquier, N., Blot, B., Laporte, M., Fraboulet, S., Coute, Y., Devoy, A., Isaacs, A.M., et al. (2015). Regulation of postsynaptic function by the dementia-related ESCRT-III subunit CHMP2B. J. Neurosci. *35*, 3155–3173.

Cho, H.J., Liu, G., Jin, S.M., Parisiadou, L., Xie, C., Yu, J., Sun, L., Ma, B., Ding, J., Vancraenenbroeck, R., et al. (2013). MicroRNA-205 regulates the expression of Parkinson's disease-related leucine-rich repeat kinase 2 protein. Hum. Mol. Genet. *22*, 608–620.

Corder, E.H., Saunders, A.M., Strittmatter, W.J., Schmechel, D.E., Gaskell, P.C., Small, G.W., Roses, A.D., Haines, J.L., and Pericak-Vance, M.A. (1993). Gene dose of apolipoprotein E type 4 allele and the risk of Alzheimer's disease in late onset families. Science *261*, 921–923.

Dodson, M.W., Zhang, T., Jiang, C., Chen, S., and Guo, M. (2012). Roles of the *Drosophila* LRRK2 homolog in Rab7-dependent lysosomal positioning. Hum. Mol. Genet. *21*, 1350–1363.

Ehrlich, M., Hallmann, A.L., Reinhardt, P., Arauzo-Bravo, M.J., Korr, S., Ropke, A., Psathaki, O.E., Ehling, P., Meuth, S.G., Oblak, A.L., et al. (2015). Distinct neurodegenerative changes in an induced pluripotent stem cell model of frontotemporal dementia linked to mutant TAU protein. Stem Cell Rep. *5*, 83–96.

Ghazi-Noori, S., Froud, K.E., Mizielinska, S., Powell, C., Smidak, M., de Marco, M.F., O'Malley, C., Farmer, M., Parkinson, N., Fisher, E.M.C., et al. (2012). Progressive neuronal inclusion formation and axonal degeneration in CHMP2B mutant transgenic mice. Brain *135*, 819–832.

Greggio, E., Jain, S., Kingsbury, A., Bandopadhyay, R., Lewis, P., Kaganovich, A., van der Brug, M.P., Beilina, A., Blackinton, J., Thomas, K.J., et al. (2006). Kinase activity is required for the toxic effects of mutant LRRK2/dardarin. Neurobiol. Dis. *23*, 329–341.

Holm, I.E., Englund, E., Mackenzie, I.R., Johannsen, P., and Isaacs, A.M. (2007). A reassessment of the neuropathology of frontotemporal dementia linked to chromosome 3. J. Neuropathol. Exp. Neurol. *66*, 884–891.

Isaacs, A.M., Johannsen, P., Holm, I., and Nielsen, J.E. (2011). Frontotemporal dementia caused by CHMP2B mutations. Curr. Alzheimer Res. *8*, 246–251.

Jiang, Q., Lee, C.Y., Mandrekar, S., Wilkinson, B., Cramer, P., Zelcer, N., Mann, K., Lamb, B., Willson, T.M., Collins, J.L., et al. (2008). ApoE promotes the proteolytic degradation of Abeta. Neuron *58*, 681–693.

Laskowitz, D.T., Thekdi, A.D., Thekdi, S.D., Han, S.K., Myers, J.K., Pizzo, S.V., and Bennett, E.R. (2001). Downregulation of microglial activation by apolipoprotein E and apoE-mimetic peptides. Exp. Neurol. *167*, 74–85.

Maki, R.A., Tyurin, V.A., Lyon, R.C., Hamilton, R.L., DeKosky, S.T., Kagan, V.E., and Reynolds, W.F. (2009). Aberrant expression of myeloperoxidase in astrocytes promotes phospholipid oxidation and memory deficits in a mouse model of Alzheimer disease. J. Biol. Chem. *284*, 3158–3169.

Martinez, E., Navarro, A., Ordonez, C., Del Valle, E., and Tolivia, J. (2012). Amyloid-beta25-35 induces apolipoprotein D Synthesis and growth arrest in HT22 hippocampal cells. J. Alzheimers Dis. *30*, 233–244.

Mwanjewe, J., and Grover, A.K. (2004). Role of transient receptor potential canonical 6 (TRPC6) in non-transferrin-bound iron uptake in neuronal phenotype PC12 cells. Biochem. J. *378*, 975–982.

Nguyen, H.N., Byers, B., Cord, B., Shcheglovitov, A., Byrne, J., Gujar, P., Kee, K., Schule, B., Dolmetsch, R.E., Langston, W., et al. (2011). LRRK2 mutant iPSC-derived DA neurons demonstrate increased susceptibility to oxidative stress. Cell Stem Cell *8*, 267–280.

Nielsen, T.T., Mizielinska, S., Hasholt, L., Isaacs, A.M., and Nielsen, J.E. (2012). Reversal of pathology in CHMP2B-mediated frontotemporal dementia patient cells using RNA interference. J. Gene Med. *14*, 521–529.

Ran, F.A., Hsu, P.D., Wright, J., Agarwala, V., Scott, D.A., and Zhang, F. (2013). Genome engineering using the CRISPR-Cas9 system. Nat. Protoc. *8*, 2281–2308.

Rasmussen, M.A., Holst, B., Tumer, Z., Johnsen, M.G., Zhou, S.L., Stummann, T.C., Hyttel, P., and Clausen, C. (2014). Transient p53 suppression increases reprogramming of human fibroblasts without affecting apoptosis and DNA damage. Stem Cell Rep. *3*, 404–413.

Rawson, R.L., Yam, L., Weimer, R.M., Bend, E.G., Hartwieg, E., Horvitz, H.R., Clark, S.G., and Jorgensen, E.M. (2014). Axons degenerate in the absence of mitochondria in *C. elegans*. Curr. Biol. *24*, 760–765.

Rossor, M.N., Fox, N.C., Mummery, C.J., Schott, J.M., and Warren, J.D. (2010). The diagnosis of young-onset dementia. Lancet Neurol. *9*, 793–806.

Urwin, H., Authier, A., Nielsen, J.E., Metcalf, D., Powell, C., Froud, K., Malcolm, D.S., Holm, I., Johannsen, P., Brown, J., et al. (2010). Disruption of endocytic trafficking in frontotemporal dementia with CHMP2B mutations. Hum. Mol. Genet. *19*, 2228–2238.

Wang, X., Yan, M.H., Fujioka, H., Liu, J., Wilson-Delfosse, A., Chen, S.G., Perry, G., Casadesus, G., and Zhu, X. (2012). LRRK2 regulates mitochondrial dynamics and function through direct interaction with DLP1. Hum. Mol. Genet. *21*, 1931–1944.

Xie, Y., Zhou, B., Lin, M.Y., Wang, S., Foust, K.D., and Sheng, Z.H. (2015). Endolysosomal deficits augment mitochondria pathology in spinal motor neurons of asymptomatic fALS mice. Neuron *87*, 355–370.

Stem Cell Reports, Volume *8*

Supplemental Information

Patient iPSC-Derived Neurons for Disease Modeling of Frontotemporal Dementia with Mutation in *CHMP2B*

Yu Zhang, Benjamin Schmid, Nanett K. Nikolaisen, Mikkel A. Rasmussen, Blanca I. Aldana, Mikkel Agger, Kirstine Calloe, Tina C. Stummann, Hjalte M. Larsen, Troels T. Nielsen, Jinrong Huang, Fengping Xu, Xin Liu, Lars Bolund, Morten Meyer, Lasse K. Bak, Helle S. Waagepetersen, Yonglun Luo, Jørgen E. Nielsen, The FReJA Consortium, Bjørn Holst, Christian Clausen, Poul Hyttel, and Kristine K. Freude

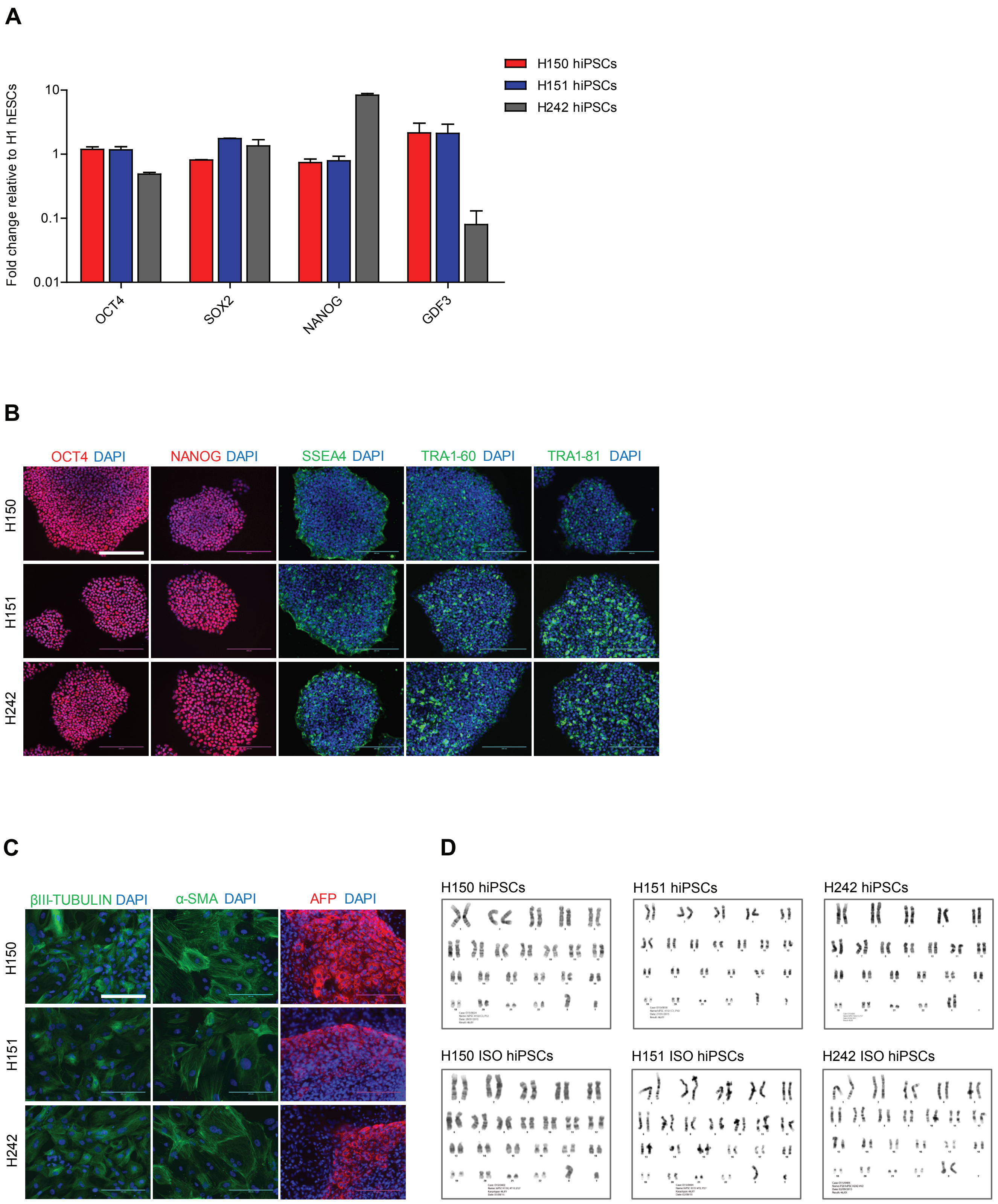
A
H150 hiPSCs
H151 hiPSCs
H242 hiPSCs
Fold change relative to H1 hESCs
10
1
0.1
0.01
OCT4
SOX2
NANOG
GDF3
B
OCT4 DAPI
NANOG DAPI
SSEA4 DAPI
TRA1-60 DAPI
TRA1-81 DAPI
H150
H151
H242
C
βIII-TUBULIN DAPI
α-SMA DAPI
AFP DAPI
H150
H151
H242
D
H150 hiPSCs
H151 hiPSCs
H242 hiPSCs
H150 ISO hiPSCs
H151 ISO hiPSCs
H242 ISO hiPSCs

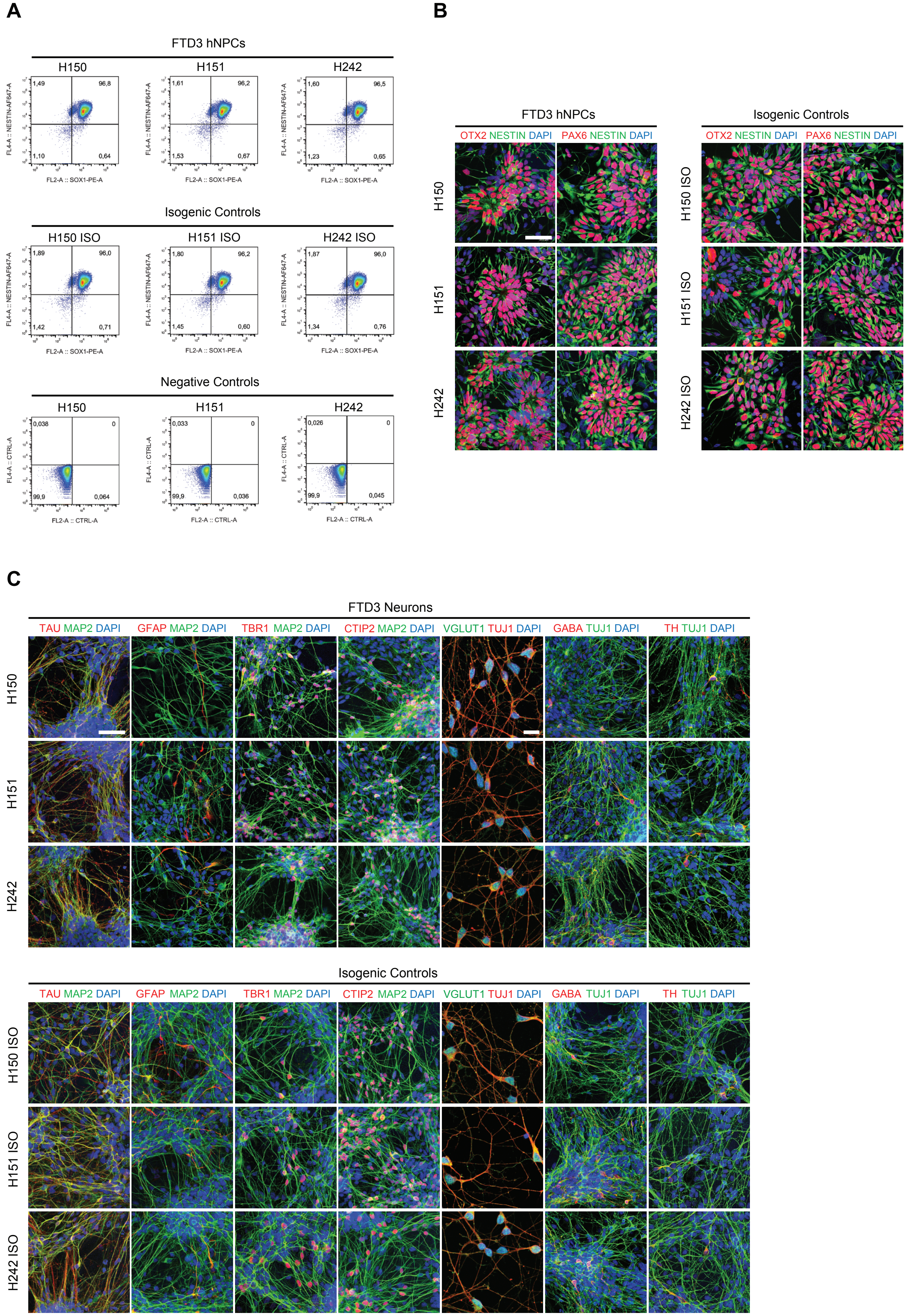A
FTD3 hNPCs
H150
H151
H242
1,49
96,8
1,10
0,64
1,61
96,2
1,53
0,67
1,60
96,5
1,23
0,65
FL4-A :: NESTIN-AF647-A
FL2-A :: SOX1-PE-A
Isogenic Controls
H150 ISO
H151 ISO
H242 ISO
1,89
96,0
1,42
0,71
1,80
96,2
1,45
0,60
1,87
96,0
1,34
0,76
Negative Controls
H150
H151
H242
0,038
0
99,9
0,064
0,033
0
99,9
0,036
0,026
0
99,9
0,045
FL4-A :: CTRL-A
FL2-A :: CTRL-A
B
FTD3 hNPCs
Isogenic Controls
OTX2 NESTIN DAPI
PAX6 NESTIN DAPI
H150
H151
H242
H150 ISO
H151 ISO
H242 ISO
C
FTD3 Neurons
TAU MAP2 DAPI
GFAP MAP2 DAPI
TBR1 MAP2 DAPI
CTIP2 MAP2 DAPI
VGLUT1 TUJ1 DAPI
GABA TUJ1 DAPI
TH TUJ1 DAPI
H150
H151
H242
Isogenic Controls
TAU MAP2 DAPI
GFAP MAP2 DAPI
TBR1 MAP2 DAPI
CTIP2 MAP2 DAPI
VGLUT1 TUJ1 DAPI
GABA TUJ1 DAPI
TH TUJ1 DAPI
H150 ISO
H151 ISO
H242 ISO

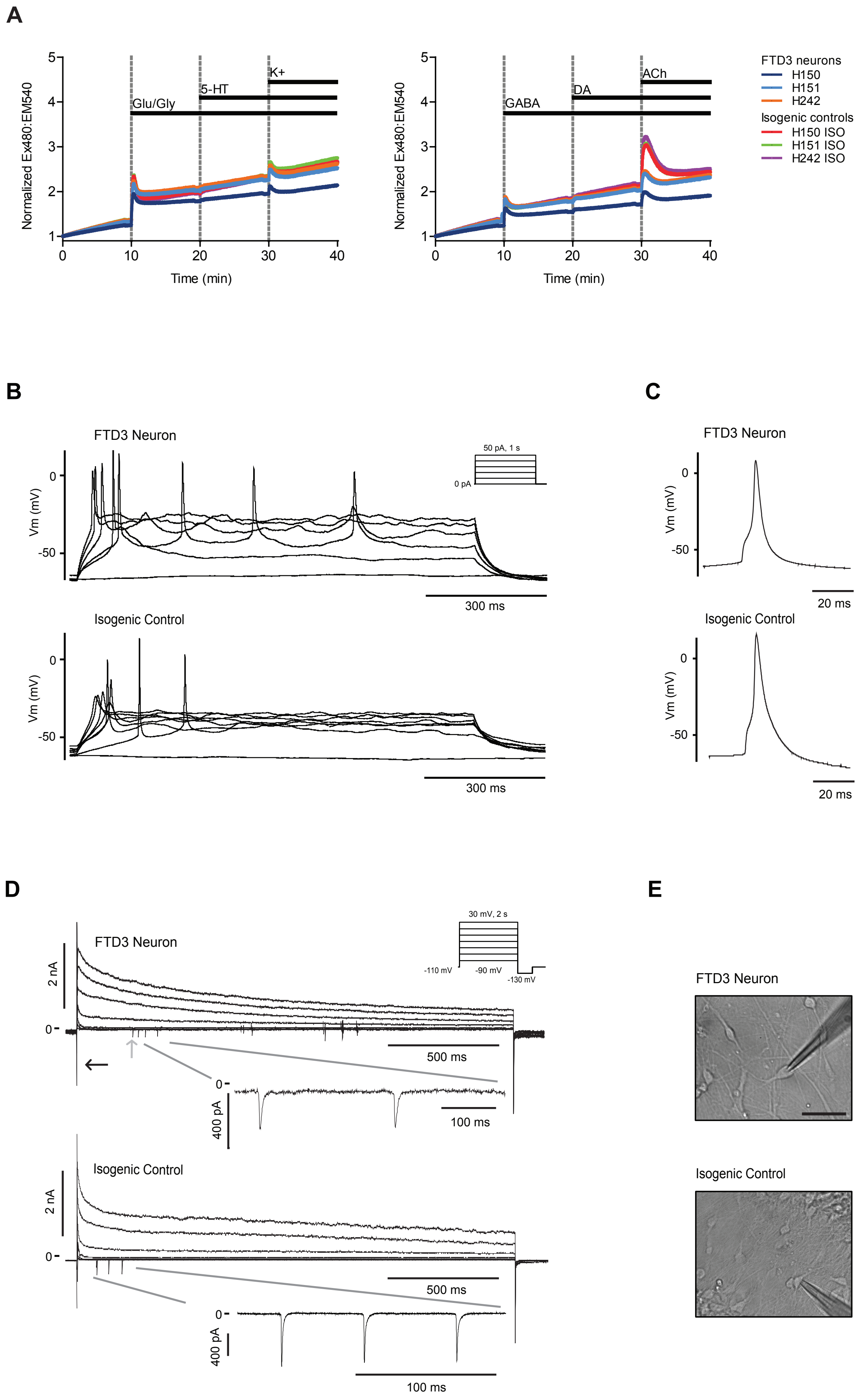
A
Normalized Ex480:EM540
Time (min)
Glu/Gly
5-HT
K+
GABA
DA
ACh
FTD3 neurons
H150
H151
H242
Isogenic controls
H150 ISO
H151 ISO
H242 ISO
B
FTD3 Neuron
Vm (mV)
0
-50
50 pA, 1 s
0 pA
300 ms
Isogenic Control
C
FTD3 Neuron
20 ms
Isogenic Control
D
FTD3 Neuron
2 nA
30 mV, 2 s
-110 mV
-90 mV
-130 mV
500 ms
400 pA
100 ms
Isogenic Control
E
FTD3 Neuron
Isogenic Control

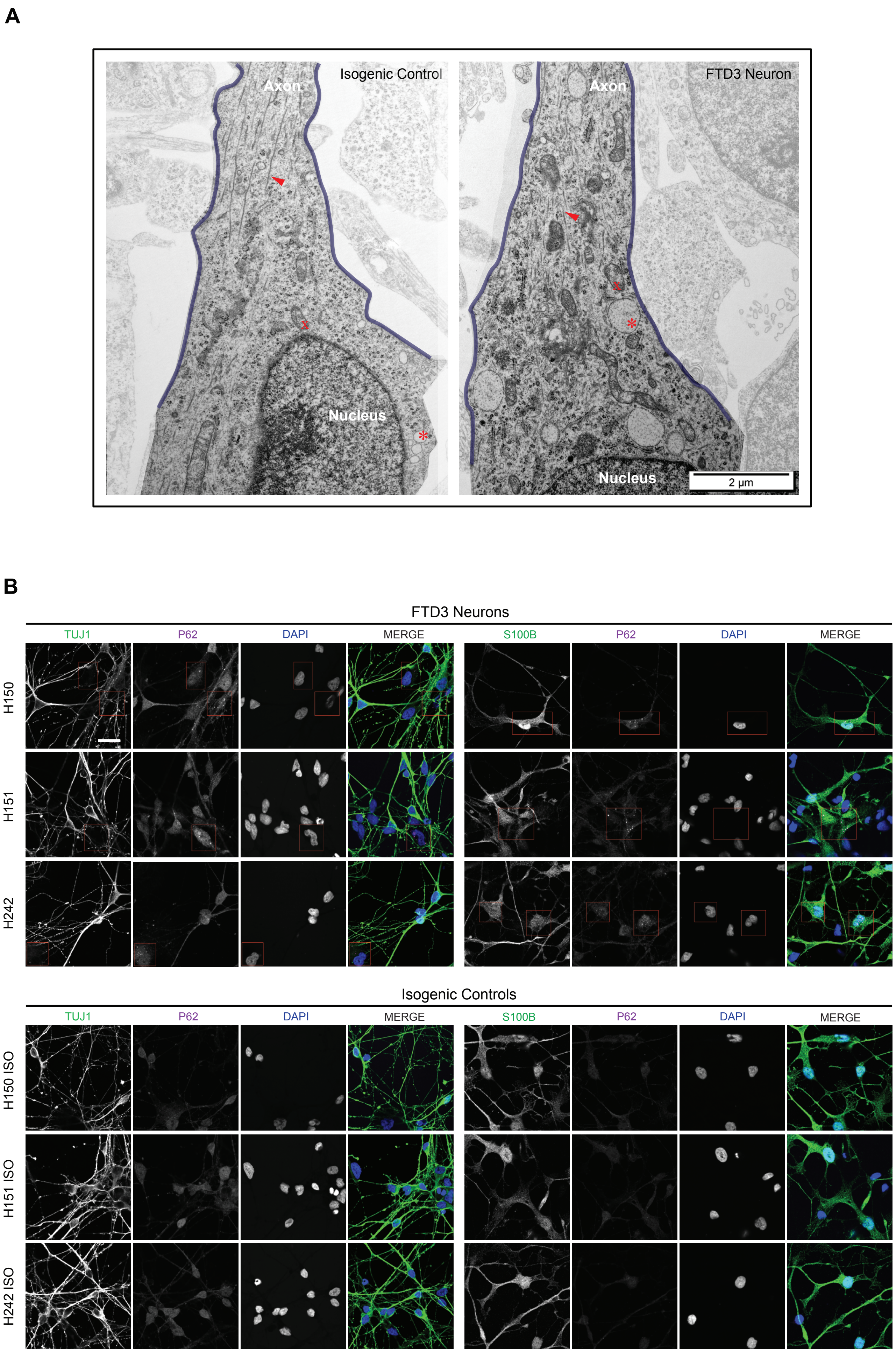
A
Isogenic Control
Axon
Nucleus
FTD3 Neuron
Axon
Nucleus
2 µm
B
FTD3 Neurons
TUJ1
P62
DAPI
MERGE
S100B
P62
DAPI
MERGE
H150
H151
H242
Isogenic Controls
TUJ1
P62
DAPI
MERGE
S100B
P62
DAPI
MERGE
H150 ISO
H151 ISO
H242 ISO

SUPPLEMENTAL FIGURE LEGENDS

Figure S1. Basic Characterisation of iPSCs, Related to Figure 1. (A) qPCR analysis of pluripotency genes in FTD3 iPSCs relative to H1 human ESCs. **(B)** ICC of FTD3 iPSCs for pluripotentcy marker proteins. Scale bars, 200 µm for all. **(C)** ICC of FTD3 iPSCs with βIII-TUBULIN (ectoderm), α-SMA (mesoderm), and AFP (endoderm) after EB differentiation. Scale bar, 200 µm for all. **(D)** Karyotype analysis of FTD3 iPSCs and isogenic controls showing no abnormalities.

Figure S2. Forebrain Identity of NPCs and Differentiation into Cortical Neurons, Related to Figure 1. (A) Flow cytometry assay for NESTIN and SOX1 in the FTD3 NPCs and isogenic controls. **(B)** Immunocytochemistry (ICC) assay of NPCs for NESTIN and forebrain progenitor protein markers OTX2 and PAX6. Scale bar, 50 µm. **(C)** ICC confocal images of FTD3 neurons and isogenic controls: dendritic neuronal protein marker MAP2 coupled with axonal protein marker TAU, glial marker GFAP, cortical markers TBR1 and CTIP2, axonal neuronal protein marker TUJ1 coupled with glutamatergic neuron marker VGLUT1, GABAergic neuron marker GABA and dopaminergic marker TH. Scale bars, 50 µm for all and 15 µm for TUJ1 coupled with VGLUT1.

Figure S3. Functional Characterization of Cortical Neurons, Related to Figure 1. (A) Intracellular calcium kinetics in FTD3 neurons (H150, H151, H242) and isogenic controls (H150 ISO, H151 ISO, H242 ISO). **(B)**, **(C)**, **(D)** and **(E)** Electrophysiological properties of FTD3 neurons and isogenic controls: **(B)** action potentials activated by current steps; **(C)** spontaneous elicited action potentials; **(D)** whole-cell currents activated by a series of voltage steps: in some recordings, excitatory postsynaptic potentials (EPSP) were observed at negative potentials as demonstrated in the enlarged portion of the recording; **(E)** representative image of patched cells. Scale bar, 300 µm for all.

Figure S4. TEM Overview Image of Neurons and p62 Aggregates Characterization in the Neural Culture, Related to Figure 2-4. (A) Images represent initial segment of an axon and a portion of the nucleus. In the FTD3 neurons, endosome-like structures (*) and mitochondria (x) accumulate, and the arrangement of microtubule structures (indicated by triangle arrow) is perturbed compared with isogenic controls. Scale bar, 2 µm for all. **(B)** Immunostaining for p62 and the neuronal marker protein TUJ1, glial maker protein S100β in FTD3 neural cultures and isogenic control. Red box indicates area with cells having p62 positive aggregates. DAPI was used a nuclear marker. Scale bar, 20 µm for all.

Table 1A

Summary of Characterization of All hiPSC Lines Used in The Current Study				
hiPSC Line	**Genotype**	**Karyotype**	**Pluripotency-associated Marker**	**Gender**
H150	G/C 31449 in *CHMP2B*	Normal	+	M
H151	G/C 31449 in *CHMP2B*	Normal	+	M
H242	G/C 31449 in *CHMP2B*	Normal	+	F
H150 ISO	Gene correction	Normal	+	M
H151 ISO	Gene correction	Normal	+	M
H242 ISO	Gene correction	Normal	+	F
H256 C6	Wild-type	Normal	+	M

Table 1B

Primers for qPCR			
Gene Name	**Gene ID (GI)**	**Forward**	**Reverse**
OCT4	553727227	CCCCAGGGCCCCATTTTGGTACC	ACCTCAGTTTGAATGCATGGGAGAGC
SOX2	325651854	TTCACATGTCCCAGCACTACCAGA	TCACATGTGTGAGAGGGGCAGTGTGC
NANOG	663071048	AAAGAATCTTCACCTATGCC	GAAGGAAGAGGAGAGACAGT
GDF3	10190669	TGACCATCTCCCTCAACAGC	TACCCACACCCACACTCATC
TRPC6	170014741	ATCCAGTCATGACGGCTTTAG	TCTGCACAGATCAAGGAGTC
HFE	91718876	TGTTCACTGTTGACTTCTGGAC	ATCATACCCGTACTTCCAGTAG
HO-1	298676487	ATGGAGCGTCCGCAACCCGAC	TGAAGCCGTCTCGGGTCACCTG
ABCG2	62526032	ACAGCTTCCAATGACCTGAA	GTTGAGACCAGGTTTCATGA

		GG	TC
FLVCR2	190341090	ACATTGAAGACCGGGACGAGC	TCAAGGCATAGCTCAGGGATTG
CP	189458860	TGGGATTATGCCTCTGACCATG	AGGTTTCATCTGTGTACTGAAG
HP	531034758	ACTCGTCCCTATACCATCCAC	TTCTGGAATGGTCCAGTTGTAG
APOE	705044057	TGGTCACATTCCTGGCAGGATG	TAATCCCAAAAGCGACCCAGTG
LRRK2	171846277	TCACGTACTCCGAGCGCGCCTC	CTGCTGCACACTCGCGACTCTC
GAPDH	576583510	ACCACAGTCCATGCCATCAC	TCCACCACCCTGTTGCTGTA
EIF6A	392494081	AAGTCTTCAGACAGACAGTGGCCGACCAG	ACCACCATCCCAGCAGCAATCACCT
CHMP2B	170650589	Common forward primer: GACATCTTTGACGGTTCTGA	
CHMP2B			Wild-type specific reverse primer: GAGCTTTGGCCATCTTTC
CHMP2B			Intron5 specific reverse primer: GAAAAGATGATGTTCATACCTTTC
CHMP2B			Delta10 specific reverse primer: CAGCTGATGGAGCTTTCC

Table 1C

List of Antibodies		
Antibody Name	**Diliution**	**Vendor and Catalog Number**
OCT4	1/500	Santa Cruz, sc-8628
NANOG	1/500	Peprotech, 500-P236
SSEA4	1/100	Biolegend, 330402
TRA-1-60	1/200	Biolegend, 330602
TRA-1-81	1/200	Biolegend, 330702

NESTIN	1/1000	Millipore, MAB5326
OTX2	1/500	R&D, AF1979
PAX6	1/300	Covance, PRB-278P
MAP2	1/500	Sigma, M1406
TUJ1	1/500	Covance, MRB-435P
TAU	1/200	Dako, A0024
GFAP	1/400	Dako, Z0334
TBR1	1/300	Abcam, ab31940
CTIP2	1/200	Abcam, ab28448
VGLUT1	1/500	Synaptic Systems, 135303
GABA	1/200	Sigma, A2052
TH	1/500	Pel-Freez Biologicals, P40101-0
S100β	1/1000	Abcam, ab11178
P62	1/200	Progen, GP62-C
TRPC6	1/1200	Alomone Labs, ACC-017
β-Actin	1/5000	Sigma, A5441
IRDye® 680LT	1/15000	LI-COR, 926-68023
IRDye® 800CW	1/15000	LI-COR, 32212

SUPPLEMENTAL EXPERIMENTAL PROCEDURES

Ethical Statement

The study was approved by the Ethics Committee of the Capital Region of Denmark (H-4-2011-157), and written informed consent was obtained from each participant before enrollment.

Cell Culture, iPSC Generation and Neuronal Differentiation

Human dermal fibroblasts cultures were obtained from skin biopsies from two symptomatic (H150, H151) and one presymptomatic (H242) FTD3 individuals (all from the same family), as well as one healthy unrelated individual (H256). The FTD3 individuals were carriers of the G-to-C transition at the 5′ acceptor splice site of *CHMP2B* exon 6 on chromosome 3 (Skibinski et al., 2005). Fibroblasts were cultured in DMEM supplemented with 1% GlutaMAX^{TM}, 10% FBS and 1% Penicillin-Streptomycin. For the generation of iPSCs, one microgram of reprogramming plasmid mixtures was electroporated into 1×10^5 fibroblasts using the Neon$^{®}$ transfection system (Thermo Fisher Scientific, USA) with a 10µL kit according to the manufacturer's instructions. The plasmid mixtures used in this experiment were pCXLE-hOCT3/4, pCXLE-hSK and pCXLE-hUL (Addgene, 27077, 27078, 27080) (Okita et al., 2011). Electroporation conditions were as followed: 1,200 V, 20 ms, 2 time pulses. After transfection, 5×10^4 cells were distributed onto 35-mm dishes coated with Matrigel (BD Biosciences, USA) and cultured in DMEM, 1% GlutaMAX^{TM}, 10% FBS without bFGF and Penicillin-Streptomycin. The culture medium was replaced the next day and supplemented with bFGF, Penicillin-Streptomycin and cultured at 5% O_2, 5% CO_2 and 90% N_2. On day 3 to 4 depending on confluence, the culture medium was replaced with ESC medium consisting of Essential 8^{TM} basal medium with supplement (Thermo Fisher Scientific, A1517001), 100 µM Sodium Butyrate and 0.1% Penicillin-Streptomycin. The colonies were manually picked 21–28 d after plating, and those colonies morphologically similar to human embryonic stem cells (ESCs) were selected for further cultivation and evaluation. When confluent, iPSC were passaged 1:3-6 with 0.5 mM EDTA on to Vitronectin^{TM} (Thermo Fisher Scientific, A14700)-coated 6-well dishes. The hiPSC clones used in this study are summarized in Table S1A. Mutation status was confirmed by Sanger sequencing.

iPSC lines were differentiated toward neural-specific progenies in 6-well plate wells (NUNC, USA) pre-coated with Matrigel® (BD Biosciences, 354277) in a 21% O_2 5.0% CO_2 37°C incubator employing a modified dual SMAD protocol (Shi et al., 2012). Cells were expanded in E8 medium until around 100% confluence was reached. Neural induction was initiated by changing the medium to neural basic medium consisted of 50% DMEM/F-12 medium, 50% Neural basal medium (Thermo Fisher Scientific, 10888-022), N2 (Thermo Fisher Scientific, 17502-048), B27 without Vitamin A (Thermo Fisher Scientific, 12587-010), supplemented with SB431542 a small molecule inhibitor of the TGFß pathway (Selleck, S1067) and LDN193189 an inhibitor of the BMP pathway (Selleck, S2618). The duration of this initial neural induction was 10 to 12 days. Subsequently, cells were split onto poly-O-Lysine/laminin (Sigma, L2020) pre-coated 6-well plate wells and remained in the neural induction medium overnight. Expansion of the neural progenitor cells, for cryopreservation and subsequent terminal differentiation was achieved by proliferating these cells in neural basic medium supplemented with 10 ng/ml bFGF. Neuronal maturation was achieved by addition of the following media: Neural basic medium supplemented with 20 ng/ml BDNF (Cell Guidance Systems, GFH1-10), 10 ng/ml GDNF (Cell Guidance Systems, GFH2-10), 50 µM db-cAMP (Sigma, D0627) and 200 µM L-Ascorbic acid 2-phosphate (Sigma, A8960). One week after terminal differentiation cells were replated again for further maturation.

Genome Editing

Generation of isogenic controls was achieved via the CRISPR/Cas9 system using single-strand donor oligonucleotides (ssODNs) as templates for single nucleotide repairs.

Isogenic gene-corrected controls were obtained using the CRISPR/Cas9 system in combination with ssODNs as homologous templates covering the mutation site. The ssODNs were designed with silent mutations that both prevent recutting of the CRISPR/Cas9 and create a restriction enzyme recognition site for SacII to enable screening for recombinant clones. The CRISPR/Cas9 vectors were generated following the protocol from Ran et al. (Ran et al., 2013). At a confluency of 80%, the iPS cells growing in a 10-cm plate were incubated with Accutase for 5 – 10 minutes at 37 °C. iPS cells were harvested and centrifuged. 2 million cells were co-transfected with 10 µg of the CRISPR/Cas9 plasmid (Addgene, 62988) and 1 µL of 100 ng/µL of the ssODNs. We used a 4D nucleofector (program CA167) from Amaxa in combination with the P3 Primary Cell Kit for transfection. Transfected cells were plated on a 10 cm dish coated with Matrigel. After one day, Puromycin (Thermo Fisher Scientific, A1113803) was added for 2 days in a 1:50000 dilution. After selection, Puromycin was withdrawn. Around 4 - 8 days after selection, resistant iPS colonies were picked and transferred to a cell culture 96 well plate. When the wells became confluent, iPS cells were split into a DNA isolation plate and a 96 well cell culture dish for further cultivation. DNA was isolated using the prepGEM™ Kit (zyGEM, PTI0500). Subsequently, a PCR was performed with primer pair P1-FW and P1-RV. PCR products were digested with SacII for 30 – 60 minutes at 37 °C. Positive clones were sequenced to confirm gene-editing of *CHMP2B*.

Quantitative qPCR

RNA was extracted using RNeasy® Plus Mini Kit (Qiagen, 74134) according to the manufacturer’s protocol. cDNA was synthesized from 1 µg of total RNA in 20 µL reaction using iScript™ cDNA synthesis Kit (BIO-RAD, 1708890). After synthesis, the cDNA was diluted five times with double distilled water and stored at −20 °C. Quantitative RT-PCR (qPCR) reactions were done in triplicates using the FastStart Lightcycler 480 SYBR Green I Master (Roche, 04707516001) on LightCycler® 480 real-time PCR system (Roche, Switzerland). cDNA samples were subjected to PCR amplification with primers for *OCT4*, *SOX2*, *NANOG*, *GDF3* and *GAPDH* (**Table S1B**). A commercial ESCs line H1 (Wicell, USA) was used as a positive control.

Quantification of *CHMP2B* RNA Transcripts

Half a microgram of RNA was subjected to first strand synthesis using random hexamer primers and SuperScript III Reverse Transcriptase (Invitrogen) in accordance with the manufacturer's instructions. PCR reactions were assembled using 5 µl of Brilliant III ultra-fast SYBR Green qPCR master mix (Agilent Technologies), 0.5 µl of forward primer (10 µM 0.5 µl of reverse primer (10 mM), 2 µl of water, and 2 µl of cDNA template. The PCR program was as follows: 2 min at 50˚C, 10 min at 95˚C and then 40 cycles of 15 s at 95˚C, 30 s at 58-60˚C (dependent on primers) and 1min at 72˚C. To distinguish the three different isoforms of *CHMP2B*, a common forward primer was used with either one of the three isoform specific reverse primers. The sequences of the primers were listed in Table S1B. For normalization, primers detecting the housekeeping gene *EIF6* were used. *CHMP2B* specific primers were used at an annealing temperature of 58˚C, whereas the *EIF6A* primer pair was used at 60˚C.

The relative abundance of the *CHMP2B* WT transcript between the different cell lines was calculated by normalization to EIF6 employing the relative standard curve method. The relative abundance of the three different isoforms of *CHMP2B* within each cell line was calculated by constructing standard curves from serial dilutions of a single plasmid holding all three amplicons in a stoichiometry of 1:1:1. This way we were able to calculate the exact amount of each isoform in relation to one another within in each cell line using the relative standard curve method.

Immunocytochemistry and Confocal Microscopy

For the immunofluorescence staining, cells were fixed with 4% formaldehyde in Dulbecco's Phosphate-Buffered Saline (DPBS) for 15 min, permeabilized with 1% Triton X-100 in DPBS for 15 min, and blocked with 2% bovine serum albumin in DPBS for 1 h. Thereafter, cells were incubated with the following primary antibodies (Table S1C) for 1 h. Primary antibodies were detected using secondary antibodies conjugated to Alexa Fluor 488 (1:500; Molecular Probes), Alexa Fluor 594 (1:500; Molecular Probes) and Alexa Fluor 647 (1:500; Molecular Probes). Cells were washed in DPBS and stained with DAPI (Sigma-Aldrich, D9542). Fresh DPBS was replaced and cells were imaged immediately using sequential line scanning with a Leica TCS SP5 II inverted CLSM or Z-stack recording with a Zeiss LSM 710 CLSM equipped with UV laser, Argon laser and AOBS beam splitter.

Flow Cytometry

To verify purity and similar proportions of marker positive hNPCs from each differentiated cell line, intracellular markers of hNPCs were analyzed by flow cytometry. When the hNPCs reached 80%–90% confluence, cells were dissociated using TrypLE™ Express (Thermo Fisher Scientific, 12605010) and incubated with Fixation/Permeabilization Working Solution (eBioscience, 88-8824) at room temperature for 60 mins. After centrifuging, the supernatant was discarded and cell pellets were resuspended in 1× Permeabilization Buffer containing monoclonal antibodies against NESTIN (BD Pharmingen, 560393) and SOX1 (BD Pharmingen, 561592). After 45 min of incubation in the dark at room temperature, cells were washed with fresh 1× Permeabilization Buffer, and resuspended in Flow Cytometry Staining Buffer (eBioscience, 00-4222) at a density of 1×10^6 cells/ml. Subsequently, they were analyzed by the CSampler™ Flow Cytometer (BD

Accuri™, USA). Unlabeled samples were used as controls for gating. Data was analyzed using the FlowJo software (version 10.0).

Whole-cell Patch Clamp Recording

Whole-cell current-clamp and voltage-clamp measurements were performed on FTD3 neurons and isogenic controls after terminal differentiation from hNPCs for 5 weeks by using a MultiClamp 700B amplifier and MultiClamp Commander (Axon Instruments, Molecular Devices, USA). Patch pipettes were fabricated from borosilicate glass capillaries (1.5mm O.D., Fisher Scientific) on a gravity puller (Model PP-830, Narishige, Japan) and had a final tip resistance of 2–3 MΩ. Recordings were performed at 36±1° C in extracellular solution containing (in mM): NaCl, 125; HEPES, 10; NaH_2PO_4, 1.25; $MgCl_2$, 1; $CaCl_2•2H_2O$, 2; glucose, 25; pyruvic acid, 3 (pH 7.4, 290 mOsm) and patch pipettes were filled with intracellular solution containing (in mM): K-gluconate, 135; NaCl, 7; $MgCl_2$, 2; HEPES, 10; Na_2-ATP, 2; Na_2-GTP, 0.3 (pH 7.2, 270 mOsm). The recording conditions were modified from Shi et al., 2012 (Shi et al., 2012). Spontaneous mini excitatory/inhibitory postsynaptic or action potential activity was monitored for 1 min. The membrane potential was adjusted to approximately -60 mV followed by stepwise current injections from 0 pA to +50 pA. Voltage-clamp recordings were performed from a holding potential of −110 mV. Currents were activated by a series of depolarizing steps ranging from −90 mV to +30 mV. All analog signals were acquired at 50 kHz, filtered at 6 kHz, digitized with a Digidata 1440 converter (Axon Instruments, Molecular Devices) and stored using pClamp10 software (Axon Instruments, Molecular Devices). Recordings were corrected for a −14 mV junction potential and data were analyzed using Clampfit 10 software (Axon Instruments, Molecular Devices).

Recordings of Intracellular Calcium Kinetics

Recordings of intracellular calcium kinetics were performed on FTD3 neurons and isogenic controls after terminal differentiation from hNPCs for 5 weeks. Neurons cultured in 96-well plates were loaded for 1 h at 37°C with 100 µL of the fluorescent calcium indicator, Calcium 5 (Molecular Devices, USA) dissolved in Hanks Balanced Salt Solution (HBSS; Thermo Fisher Scientific) with 20 mM HEPES and 1.26 mM $CaCl_2$ to 1/3 of the concentration suggested by provider. Recordings were performed at 37°C in a FDSS 7000 fluorescence kinetics plate reader (Hamamatsu Photonics, Japan). The excitation wavelength was 480 nm; the emission wavelength was 540 nm and the sampling frequency 1 Hz. Compound dilutions were prepared in assay buffer and 20 µl applied with 10 min intervals. Baseline fluorescence was recorded for 10 min before application of 300 µM glutamate/10 µM glycine, 100 µM Serotonin (5-hydroxytryptamine, 5-HT), 25 mM K^+, 100 µM GABA , 100 µM Dopamine (DA), and 300 µM acetylcholine (Ach). The fluorescence was normalized to the first data point of each of the traces.

Morphometric Analyses

Images of beta tubulin III-immunoreactive cells were recorded (12 images/cell line) using a bright field microscope (×200) connected to a digital camera (Leica). Average neurite length and soma size were assessed on coded images (experimenters ´blinded´ to sample identity) using the software ImageJ (version 1.50e) and the plugin NeuronJ (version 1.4.3). Only cells displaying an intense beta tubulin III immunostaining and a neuronal morphology (well-preserved cell soma and ≥ 1 primary neurite) were included in the analyses. Results are expressed as mean values ± SEM from 129-515 neurons per cell line.

Transmission Electron Microscopy

Cells were seeded on 13 mm Thermanox™ plastic coverslips (NUNC, 174950) coated with poly-O-Lysine/laminin. Cells were fixed with 3% glutaraldehyde (Merck, 1042390250) in 0.1 M Na-phosphate buffer, pH 7.4, post-fixed in 1% osmium tetroxide in 0.1 M Na phosphate buffer, dehydrated stepwise in a graded ethanol series, and embedded in Epon (TAAB, T031). Semi-thin (2 μm) sections were cut with a glass knife (KnifeMaster II, LKB Bromma 7800) on an ultramicrotome (Leica Ultracut, Leica Microsystems, Wetzlar, Germany), stained firstly with 1% toluidine blue O (Millipore, 1159300025) and 1% Borax (LabChem, LC117101). Ultra-thin (50 nm to 70 nm) sections were sectioned with a diamond knife (Jumdi, 2 mm) on an ultramicrotome (Leica Ultracut), contrasted with 2% uranyl acetate (Polyscience, 21447) and lead citrate, and examined using a Philips CM100 transmission electron microscope equipped with a Morada camera.

Oxidative Stress Assay

Reactive oxygen species (ROS) production was quantified in FTD3 neurons and isogenic controls using CellROX® Green Flow Cytometry Assay kit (Thermo Fisher Scientific, C10492). Staining was carried out according to the manufacturer's instructions, and stained cells were dissociated from the plate using Accutase and immediately analyzed by flow cytometry using CSampler™ Flow Cytometer (BD Accuri™, USA).

Apoptosis Assay

Activated Caspases 3 and 7 in apoptotic cells was quantified in FTD3 neurons and isogenic controls using CellEvent® Caspase-3/7 Green Flow Cytometry Assay kit (Thermo Fisher Scientific, C10427). Staining was carried out according to the manufacturer's instructions, and labeled cells were dissociated from the plate using Accutase and immediately analyzed by flow cytometry using

CSampler™ Flow Cytometer (BD Accuri™, USA).

Seahorse XF^{e}96 Mitochondria Respiration Assay

Oxygen consumption rate (OCR) was measured using a Seahorse XF^{e}96 Extracellular Flux Analyzer (Seahorse Biosciences, USA). FTD3 hNPCs and isogenic controls were seeded in a Seahorse 96-well cell culture microplate at a density of 6.5×10^3 cells/well for neuronal maturation. On the day of the assay, the culture media was changed to unbuffered DMEM (pH 7.4) supplemented with 2.5 mM glucose and the cells were equilibrated for 10 min at 37 ^{o}C in a CO_2-free incubator. The pH of the reagents used to test mitochondrial function was adjusted to 7.4 on the day of assay. The OCR measurement cycle consisted of 3-min mix and 3-min measurement of the oxygen level. Test of mitochondrial function was initiated by three baseline OCR measurement cycles. These were followed by the sequential injection of the inhibitor of ATP synthase, Oligomycin (2 µM final concentration); the uncoupling agent, Carbonyl cyanide 4-(trifluoromethoxy)phenylhydrazone (FCCP, 1 µM); a mixture of the inhibitors of mitochondrial complexes I and III, Rotenone (0.5 µM) and Antimycin A (0.5 µM) with one OCR measurement cycle in between each injection and two final measurement cycles. Oxygen consumption rates were automatically recorded and calculated by the Seahorse XF^e 96 software, Wave. Subsequent to the Seahorse analysis, the protein content was measured for each well using the Pierce assay with bovine serum albumin as standard. Results are expressed as mean values ± SEM from 12 wells/plate obtained in triplicate for each condition. Mitochondrial respiration parameters were calculated as follows: *basal respiration,* non-mitochondrial respiration (minimum measurement after rotenone/antimycin injection) was subtracted from the last measurement obtained before oligomycin injection; *proton leak*, non-mitochondrial respiration was subtracted from the measurement after oligomycin injection; *maximal respiration*, measurement obtained after FCCP injection; *spare respiratory capacity*, basal respiration subtracted from maximal respiration; *ATP production*, measurement after oligomycin injection was substracted from the last measurement before oligomycin injection.

MitoTracker ® Assay

Cells for MitoTracker® Red CMXRos (Molecular Probes, M7512) analysis were cultured on 0.17 μm glass coverslips coated with poly-O-Lysine/laminin. When ready for staining, cells were incubated with 50 nM MitoTracker® in DMEM/F-12 medium for 15 min in 37 °C. Following, fixation in 4% paraformaldehyde in DPBS, permeabilization in 0.5% Triton X-100 in DPBS for 15 min, incubation with DAPI for 10 min in room temperature. In between each step the samples were washed 3 times in DPBS. After the last wash, the glass coverslips were mounted with mounting media and sealed onto slides. Images were acquired by laser scanning confocal microscopy (Zeiss LSM 710).

RNA Sequencing Analysis

For deep RNA sequencing, libraries of FTD3 neurons, isogenic controls and one independent healthy control were prepared and sequenced independently on HiSeq 2000 Sequencing System (Illumina, USA). For library construction, after extracting the total RNA from samples, mRNA and non-coding RNAs are enriched by removing rRNA from the total RNA with kit. By using the fragmentation buffer, the mRNAs and non-coding RNAs are fragmented into short fragments (about 200-500 nt), then the first-strand cDNA is synthesized by random hexamer-primer using the fragments as templates, and dTTP is substituted by dUTP during the synthesis of the second strand. Short fragments are purified and resolved with EB buffer for end reparation and single nucleotide A (adenine) addition. After that, the short fragments are connected with adapters, then the second strand is degraded using UNG(Uracil-N-Glycosylase) finally. For data processing, Illumina Casava1.8 software was used for base calling. Clean reads were obtained by filtering reads with adaptor sequences and low quality reads. Clean reads that aligned to rRNA were removed. After removing reads aligned to rRNA, we used SOAP2 to align clean reads to the hg19 UCSC RefSeq (RNA sequences, GRCh37) (para: -m 0 -x 1000 -s 40 -l 32 -v 5 -r 2 -p 4). Gene level expression was performed by transforming uniquely mapped transcript reads to TPM. Normalized differentially expressed genes were detected. Genes whose expression changes are more than 1.5 folds with FDR < 5% identified in FTD3 neurons compared to isogenic controls were submitted to Gene ontology (GO) enrichment analysis. GO enrichment analysis of assembled transcripts was performed with ClueGO v1.4 (Bindea et al., 2009) using the following parameters: use GO term fusion; enrichment/depletion two-sided hypergeometric statistical test; correction method: Benjamini-Hochberg; GO term range levels: 3-8; minimal number of genes for term selection: 10; minimal percentage of genes for term selection: 10%; κ-score threshold: 0.5; general term selection method: smallest *p* value; group method: κ; minimal number of subgroups included in a group: 3; minimal percentage of shared genes between subgroups: 50%. For qPCR validation of the RNA sequencing results, we performed independent neuronal differentiation experiments and examined key gene expression, and all primer sequences for these genes are listed in **Table S1B**.

Western Blotting

Cell pellets from FTD3 neurons and isogenic controls were lysed in mPER™ mammalian protein extraction reagent (Thermo Fisher Scientific, 78501) containing protease inhibitor (Complete tablets, Roche 11873580001) and phosphatase inhibitors (PhosSTOP tablets, Roche 04906845001). 10 μg of protein were separated by NuPAGE™ Novex™ 4-12 % Bis-Tris mini gel

(Thermo Fisher Scientific, NP0335BOX) followed by immunoblotting with rabbit anti-TRPC6 (Alomone Labs, ACC-017) and mouse anti-ß-Actin (Sigma, A5441) primary antibodies, donkey-anti-rabbit IRDye® 680LT (LI-COR, 926-68023) and donkey-anti-mouse IRDye® 800CW (LI-COR, 32212) secondary antibodies. Immunoblots were developed by Odyssey® Fc Imaging System (LI-COR) and data was processed using the software ImageStudio version 5.2.5. Expression levels of TRPC6 were normalized to ß-Actin.

Ferrous Iron Assay

Cell pellets were obtained from FTD3 neurons and isogenic controls. An iron assay kit (Abcam, ab83366) was subsequently used to quantify ferrous iron (Fe^{2+}) in the neurons according to manufacturer's instructions. Briefly, cell pellets were homogenized with 120 µL iron assay buffer and supernatants were collected. 20 µL cell supernatant was used for the assay and volume was adjusted to 100 µL with iron assay buffer. Then, 100 µL of the iron probe solution was added producing a Fe^{2+}-Ferene S complex that absorbs light at 593 nm. Infinite® 200 PRO Multimode Reader (TECAN, Switzerland) was used to detect absorbance at this wavelength.

Statistical Analysis

Data are presented as mean ± standard errors (S.E.). “n” is the number of independent differentiations of NPCs (from the cryobank) to neurons. Significance of data was evaluated by Student’s *t* test or two-way ANOVA with Bonferroni *post hoc* test. Unless noted otherwise, $P<0.05$ was considered statistically significant.

Supplemental References

Bindea, G., Mlecnik, B., Hackl, H., Charoentong, P., Tosolini, M., Kirilovsky, A., Fridman, W.H., Pages, F., Trajanoski, Z., and Galon, J. (2009). ClueGO: a Cytoscape plug-in to decipher functionally grouped gene ontology and pathway annotation networks. Bioinformatics *25*, 1091-1093.

Okita, K., Matsumura, Y., Sato, Y., Okada, A., Morizane, A., Okamoto, S., Hong, H., Nakagawa, M., Tanabe, K., Tezuka, K., *et al.* (2011). A more efficient method to generate integration-free human iPS cells. Nat Methods *8*, 409-412.

Ran, F.A., Hsu, P.D., Wright, J., Agarwala, V., Scott, D.A., and Zhang, F. (2013). Genome engineering using the CRISPR-Cas9 system. Nat Protoc *8*, 2281-2308.

Shi, Y., Kirwan, P., and Livesey, F.J. (2012). Directed differentiation of human pluripotent stem cells to cerebral cortex neurons and neural networks. Nat Protoc *7*, 1836-1846.

Skibinski, G., Parkinson, N.J., Brown, J.M., Chakrabarti, L., Lloyd, S.L., Hummerich, H., Nielsen, J.E., Hodges, J.R., Spillantini, M.G., Thusgaard, T., *et al.* (2005). Mutations in the endosomal ESCRTIII-complex subunit CHMP2B in frontotemporal dementia. Nat Genet *37*, 806-808.